Electrochemistry Communications 102 (2019) 46–51

Contents lists available at ScienceDirect

Electrochemistry Communications

journal homepage: www.elsevier.com/locate/elecom

Full communication

Vanadium phosphide–phosphorus composite as a high-capacity negative electrode for sodium secondary batteries using an ionic liquid electrolyte

Shubham Kaushik[a], Kazuhiko Matsumoto[a,b,*], Yuta Sato[c], Rika Hagiwara[a,b]

[a] Graduate School of Energy Science, Kyoto University, Sakyo-ku, Kyoto 606-8501, Japan
[b] Unit of Elements Strategy Initiative for Catalysts & Batteries (ESICB), Kyoto University, Katsura, Kyoto 615-8510, Japan
[c] Nanomaterials Research Institute, National Institute of Advanced Industrial Science and Technology (AIST), Central 5, 1-1-1 Higashi, Tsukuba, Ibaraki 305-8565, Japan

ARTICLE INFO

Keywords:
Sodium secondary battery
Vanadium phosphide–phosphorus composite
Negative electrode
Ionic liquid
Intermediate temperature

ABSTRACT

A vanadium phosphide–phosphorus composite, V_4P_7/5P, is investigated as a negative electrode for sodium-ion batteries using the ionic liquid, Na[FSA]–[C_3C_1pyrr][FSA] (FSA = bis(fluorosulfonyl)amide anion and C_3C_1pyrr = *N*-methyl-*N*-propylpyrrolidinium cation), as the electrolyte. Analyses of the X-ray diffraction pattern, X-ray photoelectron spectra, and transmission electron microscopy images revealed that the V_4P_7/5P composite prepared by high-energy ball-milling is composed of a V_4P_7 crystalline phase and an amorphous phosphorus phase. This composite exhibits a high reversible discharge capacity of 738 mAh g^{-1} with a reasonably high initial coulombic efficiency of 85.9% at 363 K, even in the absence of carbon materials. The emergence of Na_3P peaks in the ex situ XRD pattern after full charging indicated sodiation of the excess amorphous phosphorus present in the composite. The peaks corresponding to V_4P_7 remained intact and desodiation of Na_3P after full discharge was also evident from the XRD pattern. The cyclability was higher in the ionic liquid electrolyte than in an organic electrolyte owing to the formation of a more efficient interfacial layer in the former.

1. Introduction

Sodium-ion batteries (SIBs) are believed to be a suitable technology for high-energy-density and low-cost stationary energy storage systems, owing to their low standard electrode potential (−2.71 vs standard hydrogen electrode), abundance of sodium resources, and use of an aluminum current collector [1–4]. Recently, phosphorus-based compounds are being widely used as negative electrodes in SIBs owing to the high theoretical capacity (~2596 mAh g^{-1}) of elemental phosphorous, due to the formation of Na_3P after sodiation [5]. However, owing to the low electrical conductivity of phosphorus (~10^{-14} S cm^{-1}) and large change in volume during sodiation and desodiation, severe capacity fade is often observed. The difficulties arising from the large volume change can be attenuated by using metal phosphides, including Cu_3P, CuP_2, FeP_4, and Sn_4P_3, which form a conductive matrix of metal after sodiation [6–9] and by limiting the desodiation of phosphorus which was reported recently in the case of Sn_4P_3 [10]. However, the cyclability and rate capability are still limited. Although the introduction of carbon to the metal phosphide improves the rate capability and cycle performance [11,12], the tap density of the material decreases because of the low density of carbon, while the first-cycle coulombic efficiency reduced owing to the side reactions arising from the large surface area. Hence, a metal phosphide with a buffer, rather than carbon, can give a new direction for fabricating negative electrodes for SIBs.

The P–TiP_2–C composite prepared by ball-milling showed excellent cyclability and rate performance as a negative electrode for both lithium-ion batteries (LIBs) and SIBs [13]. TiP_2 could buffer against the large volume change during the sodiation/desodiation, owing to its structural stability and inactivity toward sodiation/desodiation. Vanadium phosphides (VP, V_4P_7, and VP_2) have been already investigated as negative electrodes for LIBs [14,15]; VP showed a moderate capacity with good cyclability owing to a very low volume change during cycling, while VP_2 exhibited high capacity but poor cyclability. The characteristics of V_4P_7 was intermediate between the other two phosphides, and it exhibited high capacity as well as good cyclability and rate capacity [16]. X-ray diffraction (XRD) and X-ray absorption (XAS) analyses suggest that all the aforementioned vanadium phosphides function according to an insertion mechanism. A recent study for V_4P_7 for SIBs showed excellent cyclability and rate performance [17]. This may be related to the relatively low resistivity of V_4P_7 (2×10^{-4} Ω cm) reported in [18]. However, for seeking high energy density of batteries,

* Corresponding author at: Graduate School of Energy Science, Kyoto University, Sakyo-ku, Kyoto 606-8501, Japan.
E-mail address: k-matsumoto@energy.kyoto-u.ac.jp (K. Matsumoto).

https://doi.org/10.1016/j.elecom.2019.03.014
Received 22 February 2019; Received in revised form 24 March 2019; Accepted 24 March 2019
Available online 27 March 2019

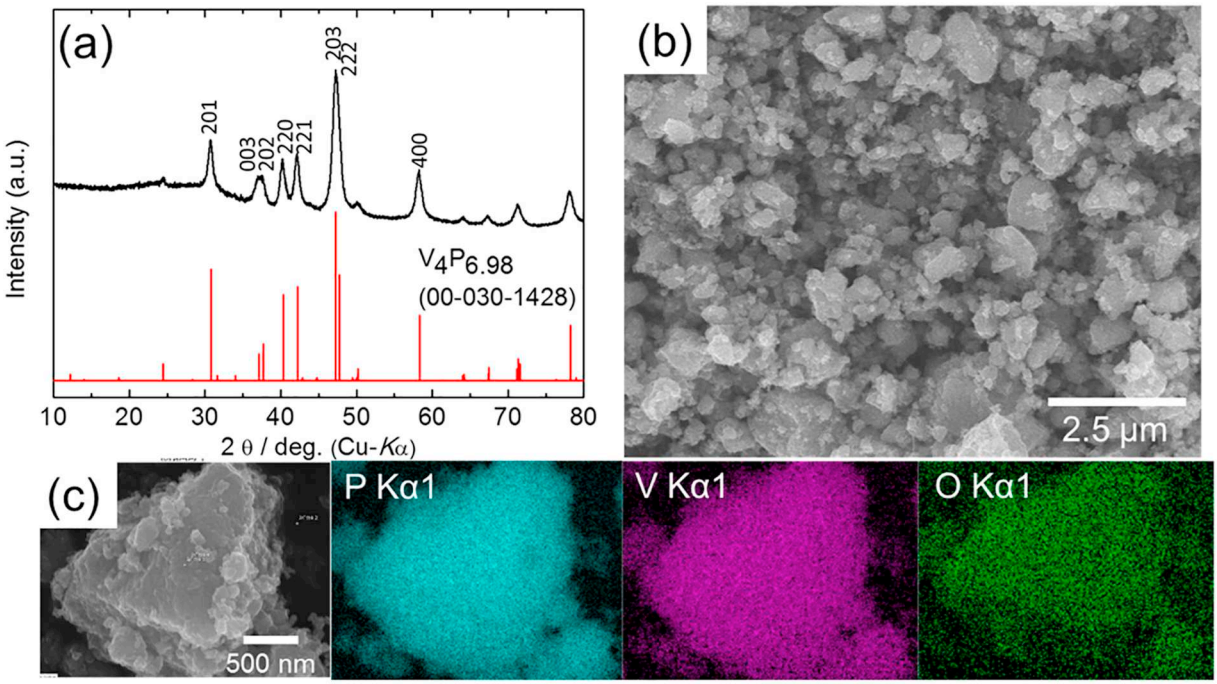

Fig. 1. (a) X-ray diffraction pattern, (b) SEM image, and (c) EDX mapping of V_4P_7/5P particles.

a higher capacity of negative electrode materials is required. Hence, it will be interesting to investigate V_4P_7/P composite for the SIBs.

Ionic liquids (ILs) have attracted widespread attention for the safety and high performance aspects owing to the negligible flammability and volatility, wide electrochemical window and high thermal stability [19,20]. Several studies in the past few years have suggested that some negative and positive electrodes exhibit better performance with ILs than with organic electrolytes [21–23]. This is partly explained by the formation of a uniform solid electrolyte interface (SEI) layer in the first cycle and suppression of large volume change in negative electrodes [24]. Another advantage of using ILs is their compatibility with operation at elevated temperatures because of their thermal stability. This is because both the diffusion of Na^+ ions and the electrode reactions are enhanced at elevated temperatures; such a temperature range above room temperature is defined as the intermediate temperature [25,26]. A recent report demonstrated a considerable reduction in the interfacial resistance at intermediate temperatures using ILs [27]. Pyrrolidinium-based binary ILs are known to provide a stable passivation layer, especially in phosphorus-based systems [28,29]. All these observations motivated us to investigate ILs as electrolytes in our study. We have investigated the vanadium phosphide–phosphorus composite, V_4P_7/5P (and analogues with different V/P ratio), as a negative electrode in SIBs at 298 and 363 K, using the ionic liquid, Na[FSA]–[C_3C_1pyrr][FSA] (FSA = bis(fluorosulfonyl)amide anion and C_3C_1pyrr = *N*-methyl-*N*-propylpyrrolidinium cation) IL [30,31], as the electrolyte.

2. Experimental

The vanadium phosphide/phosphorus composite, V_4P_7/5P, was prepared by one-step high-energy ball milling (HEBM) of vanadium metal (Kojundo Chemical Lab, purity 99.9%) and phosphorus powder (Wako Pure Chemical Industries, purity 98%) in a stoichiometric ratio (V:P = 4:12) under Ar atmosphere. The ball to powder ratio was kept at 50:1 at 400 rpm for 20 h. In order to see the effect of the V/P ratio, V_4P_7, V_4P_7/9P (V:*P* = 4:16), and V_4P_7/13P (V:P = 4:20) were prepared by HEBM in the same condition. The V_4P_7 without any excess phosphorus will be called pristine V_4P_7 in this manuscript. Based on the capacity value and capacity retention of the composites, V_4P_7/5P was chosen as the main material for investigation (Fig. S1). The XRD patterns of the samples were obtained on a Rigaku SmartLab diffractometer (Cu Kα (1.5418 Å), 40 kV − 30 mA). Particle size, morphology, structural parameters, and elemental composition were analyzed by scanning electron microscopy (SEM, Hitachi SU-8020) and scanning transmission electron microscopy (STEM, JEOL JEM-2100F). The chemical bonding states were analyzed by X-ray photoelectron spectroscopy (XPS, JEOL, JPS-9010, MgKα, 10 kV-10 mA).

The test electrodes were prepared by mixing the active material (V_4P_7, V_4P_7/5P, V_4P_7/9P, V_4P_7/13P), acetylene black (Wako Pure Chemical Industries), and a carboxymethyl cellulose/styrene-butadiene binder in a weight ratio of 75:15:5:5 in water. The resulting slurry was subsequently cast on an Al foil and dried under vacuum, first at 363 K for 10 h and then overnight at 383 K (mass loading: ~1 mg cm^{-2}). The Na[FSA]-[C_3C_1pyrr][FSA] IL was prepared by mixing the two salts (Na[FSA]: Mitsubishi Materials Electronic Chemicals Co., Ltd., purity > 99%, and [C_3C_1pyrr][FSA]: Kanto Chemical Co., Inc., purity > 99.9%), which were first vacuum-dried at 353 K in a 2:8 M ratio and further vacuum-dried at 363 K for > 10 h. A glass fiber filter (Whatman, GF-A, 260 mm in thickness and 16 mm in diameter) was used as a separator, and a sodium metal disc (Aldrich, purity 99.9%) was used as the counter electrode. Electrochemical performance was tested by assembling a 2032 coin cell under Ar atmosphere. For ex situ XRD measurements, the electrodes were taken out of the coin cells in both the charged and discharged states, rinsed with tetrahydrofuran, and vacuum-dried for one day at room temperature. The electrochemical impedance spectroscopy measurements were performed with a VSP potentiostat (Bio-Logic) at 298 and 363 K over a frequency range from 100 mHz to 100 kHz, with an AC amplitude of 20 mV.

3. Results and discussion

Fig. 1 (a) shows the XRD pattern of V_4P_7/5P prepared by HEBM. All the peaks are assigned to tetragonal V_4P_7 (space group $P-4m2$) that

has a partial occupancy of 0.75 for one of the two P sites; [18] however, a slight deviation in the stoichiometry is possible. The XRD pattern suggests the formation of a crystalline V_4P_7 phase with an amorphous red phosphorus phase (5P, considering the stoichiometry in the initial state), although the latter cannot be detected in XRD. On the other hand, the peaks of pristine V_4P_7, V_4P_7/9P, and V_4P_7/13P are also indexed to V_4P_7 (Fig. S2), suggesting the increase of the P/V ratio simply leads to the increase of the amorphous phosphorus phase. The particle size and morphology were analyzed by SEM (Fig. 1(b)). Continuous collision and fracture during ball-milling resulted in a random morphology of the particles. The size of the particles ranges from 500 nm to a few micrometers. Elemental mapping in the energy-dispersive X-ray (EDX) spectrum suggests that the elements in the V_4P_7/5P composite were uniformly distributed in the particle (Fig. 1(c)). A small amount of oxygen, as confirmed from the mapping, can be attributed to the oxidation of the elements during ball-milling owing to the high rotational speed of operation. This was further confirmed by the presence of oxide (V^{2+}) peaks around 522.1 and 513.6 eV and V^{5+} peaks (516.7 and 523.2 eV) in the V 2p XPS and at 134 eV in the P 2p XPS owing to -PO_4- bond in $VOPO_4$ (Fig. S3(a) and (b)). The peaks in V 2p and P 2p (512.7 and 130.1 eV, respectively) can be indexed to both the existence of elemental vanadium (512.6 eV), phosphorus (130.1 eV), and the formation of V_4P_7 because the binding energies values are very close to each other. Although there is no XPS data for V_4P_7, its binding energy is considered to be close to that of VP (V 2p = 512.6 and P $2p_{3/2}$ = 129.1 eV, respectively) because the binding energies of the most 3d transition metal phosphides are similar to each other (P $2p_{3/2}$ for FeP, MnP, and TiP are 129.5, 129.4, and 128.4 eV, respectively). [32]

To obtain the composition of V_4P_7/5P and to confirm the presence of excess elemental phosphorus in the amorphous structure, further characterization is required. Therefore, the high-resolution HRTEM image of the pristine powder was captured (Fig. 2(a)). The *d*-spacing of V_4P_7/5P was estimated by the fast Fourier transformation (FFT, Fig. 2(b)) of two specific regions. The results confirmed the formation V_4P_7 nanocrystallites of size 5–15 nm, embedded within the amorphous phosphorus matrix. Elemental mapping of the composite also supports this argument, as the excess phosphorus can be observed around the nanocrystallites of V_4P_7 (Fig. 2(c)). The atomic ratio of P and V, calculated for several particles by STEM-electron energy loss spectroscopy, was in the range 2.3–2.6 (Fig. S4), which is in good agreement with the ratio of the materials used for HEBM.

The electrochemical performance of the V_4P_7/5P composite with IL as the electrolyte is shown in Fig. 3. Fig. 3(a) and (b) represents the galvanostatic charge–discharge curves at 298 and 363 K, respectively, for the first three cycles at 100 mA g^{-1} in the voltage range 0.005–2 V. The curves at 298 K for the charging process (Fig. 3(a)) of the first cycle consists of a sloping profile with one indistinct plateau around 0.15 V. A high first-cycle coulombic efficiency of 88% indicates that the side reactions in the first cycle are highly suppressed in this electrode in an IL, in contrast to that reported for other negative electrodes such as hard carbon and phosphides, wherein the efficiency was typically lower than 75% [8,33]. During desodiation, all the curves for the first three cycles overlap with each other, which indicates a reversible extraction of sodium from the composite matrix. The curves obtained at 363 K (Fig. 3(b)) are indicative of lesser polarization and contains more plateaus owing to the increase in temperature. The plateau at 0.25 V is more distinct than that at 298 K for the same voltage. Details on plateau potentials are further discussed by cyclic voltammetry (Fig. S5). At 100 mA g^{-1}, the high first-cycle discharge capacities at 298 and 363 K were 560 and 738 mAh g^{-1}, respectively, while the coulombic efficiencies at 298 and 363 K were 88% and 86%, respectively. In the rate capability test at 363 K (Fig. 3(c)), this system exhibited high discharge capacities of 695, 537, and 360 mAh g^{-1} at the rates of 100, 1000, and 8000 mA g^{-1}, respectively. Even at 298 K, reasonable discharge capacities of 588, 271, and 155 mAh g^{-1} were observed at the rates of 100, 1000, and 2000 mA g^{-1} respectively. Fig. 3(d) shows the cycle performance (the first two cycles were performed at 100 mA g^{-1}) for 100 cycles at 298 K (rate = 200 mA g^{-1}) and 363 K (rate = 500 mA g^{-1}). In the fourth cycle, the discharge capacities at 298 and 363 K were 548 and 613 mAh g^{-1}, respectively, while the coulombic efficiencies at the same temperatures were 99.2% and 99.3%, respectively. The capacity increased for the first 20 cycles at 298 K owing to the activation and then gradually decreased. Cyclability test at 363 K indicated a constant capacity for few cycles, followed by a decrease in the capacity. This was similar to that observed at 298 K. After 100 cycles, the capacity retention reached 54% and 48% at 298 and 363 K, respectively, with corresponding coulombic efficiencies of 98.1% and 99.1%. The cyclability was also evaluated at 298 K using 1 M $NaPF_6$ in an organic electrolyte, ethylene carbonate/diethylene carbonate (1:1 (v/v)), in order to compare the performance with that in the IL electrolyte. The first charge–discharge curves at the rate of 100 mA g^{-1} (cut-off voltage range 0.005–2 V) delivered a discharge capacity of 605 mAh g^{-1}, with a coulombic efficiency as high as 88% (Fig. S6(a)). Although the reaction was reversible till the fifth cycle, severe capacity degradation could be observed after that (Fig. S6(b)). A similar behavior was also reported for Sn_4P_3 and phosphorous negative electrodes [28], wherein the SEI layer was found to be non-uniform in the organic electrolyte. Na[FSA]-[C_3C_1pyrr][FSA], however, provided a uniform passivation layer.

The electrochemical performance of the pristine V_4P_7 was measured at 298 and 363 K for comparison (Fig. S7(a) and Fig. S1(a)) shows the charge-discharge curves at 100 mA g^{-1} for the first three cycles at 298 and 363 K, respectively. The obtained reversible discharge capacity at 298 K with IL is 270 mAh g^{-1} (~1 Na^+ per $VP_{1.75}$ unit) which is similar to the reported value in [17] but when the temperature is raised to 363 K, the discharge capacity for first cycle reaches 470 mAh g^{-1} (1.85 Na^+ per $VP_{1.75}$ unit) with the initial coulombic efficiency of 71%. Although the pristine V_4P_7 exhibits a high cyclability, V_4P_7/5P has an advantage in capacity. Increase of phosphorus content in the composite (V_4P_7/9P, and V_4P_7/13P) increases the first cycle capacity at the cost of severe capacity fading. By considering these data, V_4P_7/5P is regarded as a well-balanced material in this series in terms of capacity and cyclability.

The charge–discharge mechanism was analyzed by ex situ XRD (Fig. 4). The rate of charging and discharging was 100 mA g^{-1}, in the cut-off voltage range 0.005–2 V. The XRD pattern of the pristine sample shows peaks corresponding to V_4P_7. There is no difference between the XRD patterns of the pristine sample and the one charged at 0.24 V. Peaks for Na_3P could be observed after charging to 0.005 V, although the peaks corresponding to V_4P_7 remained intact. This result is similar to the previous report which observed no change in the peaks of V_4P_7 [17]. Na_3P was desodiated during discharging, as evident from the decrease in the number and intensities of the XRD peaks of Na_3P at 0.54 V. The peaks ultimately disappeared at 2 V. The XRD patterns in the second cycle indicates the reversibility of the reaction. Moreover, the ex-situ XRD of the pristine V_4P_7 also supports the arguments above as there is no change in the peaks for charged and discharged samples (Fig. S8).

To see the change in resistance with cycling in different electrolytes, impedance spectra of V_4P_7/5P were measured in a half cell configuration with IL (298 and 363 K) and organic electrolytes at 298 K (Fig. S9(a), (b) (inset: magnified plot) and (c)), respectively. The V_4P_7/5P electrode was charged and discharged for one, three, and ten cycles, and then charged to 0.5 V during the next charging step. A constant decrease in the interfacial resistance till the tenth cycle is observed in IL at both 298 and 363 K, though the initial value for IL at 298 K is larger than that for organic electrolyte owing to the development of surface film between sodium metal and IL electrolyte, [27] while the interfacial

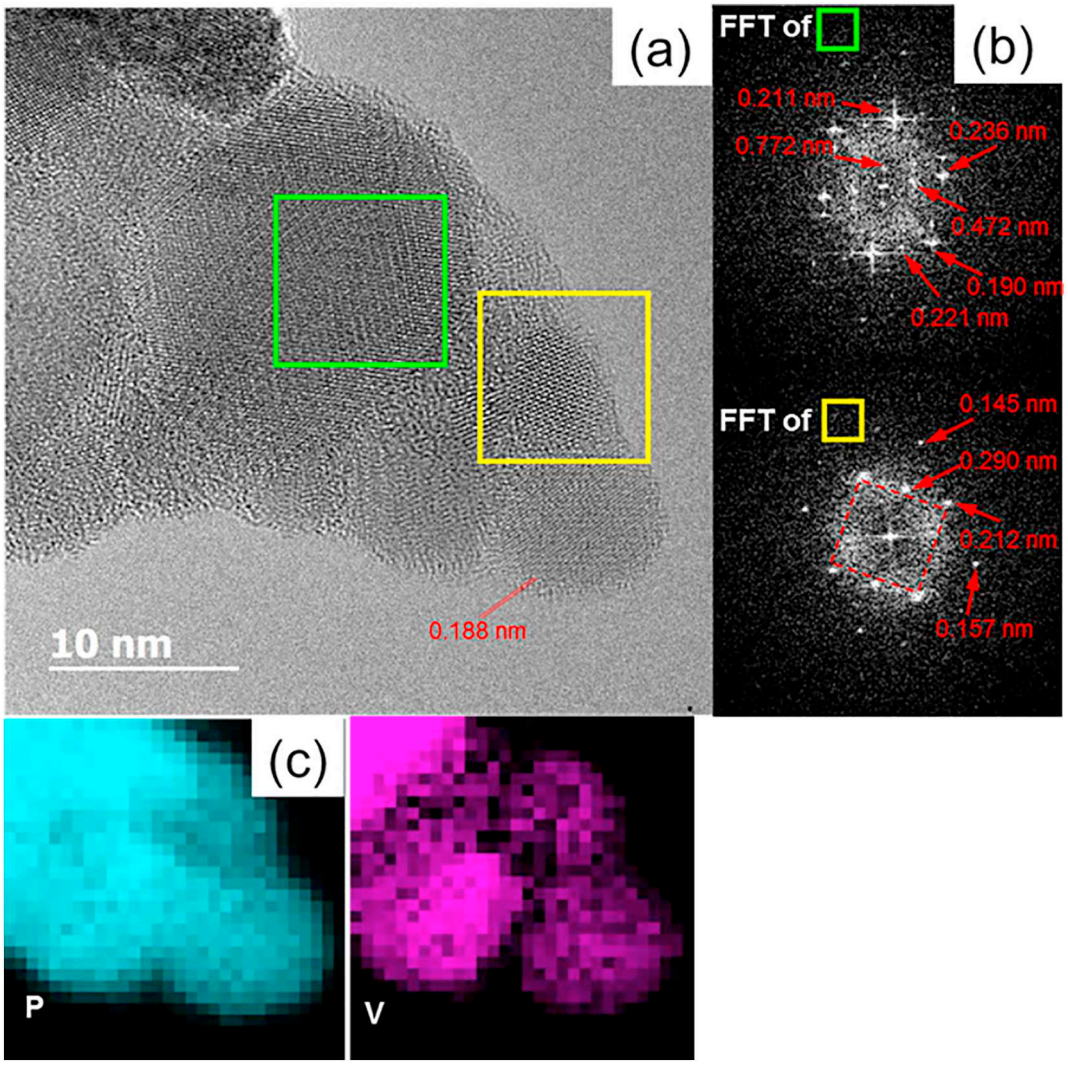

Fig. 2. (a) HRTEM of the V_4P_7/5P particles, (b) FFT of the particles in the two areas marked in (a), and (c) elemental mapping of the particles.

resistance increases drastically after the first cycle in the organic electrolyte. This correlates with the cyclability test, confirming the benefit of IL over organic electrolytes with respect to the performance. This result is further supported by the surface analysis of electrode after 10 cycles in IL and organic electrolyte by SEM (Fig. S10(b) and (c), respectively). Substantial increase in particle size is clearly evident in the case of organic electrolyte whereas, it is almost the same as pristine (Fig. S10(a)) in IL electrolyte. Similar results were obtained in case of silicon negative electrode in LIBs [24].

The enthalpy of formation [34] and reaction mechanism for some selected 3d transition metal phosphides (MP_x with low x value) used in LIBs and SIBs are summarized in Table S1. The enthalpy of formation of MP_x (per mole of the respective transition metals) increases with increasing atomic number, and titanium and vanadium phosphides have significantly small (large negative) enthalpies of formation. This prevents the conversion reaction of these phosphides with high lattice energy in both LIBs and SIBs, and it was certainly reported that V_4P_7 works based on the topotactic insertion mechanism. All the late 3d transition metal phosphides are active for the conversion reaction because of their low negative enthalpies of formation. Further discussion from the viewpoint of thermodynamics is difficult here because of the lack of reliable data.

4. Conclusions

In this study, we reported for the first time the use of a V_4P_7/5P composite as a negative electrode for SIBs, using an IL as the electrolyte. The XRD, HRTEM, SEM, and XPS analyses confirmed the formation of V_4P_7/5P and revealed the morphology and particle size. Large reversible capacities of 560 mAh g^{-1}, with a large coulombic efficiency of 88%, and 738 mAh g^{-1}, with a coulombic efficiency of 86%, were observed at 298 and 363 K, respectively, in the absence of carbon materials. A capacity of 360 mAh g^{-1} was obtained even at a high rate of 8000 mA g^{-1} at 363 K, and 47.2% capacity retention was achieved after 100 cycles. The ex situ XRD analysis revealed the reversible sodiation and desodiation of phosphorus in Na_3P and the insertion mechanism of V_4P_7 phase. The advantage of V_4P_7 is to provide mechanical integrity, electrical conductivity and capacity to the electrode for better performance. Moreover, the interfacial layer in IL was better than that in the organic electrolyte. Our results demonstrated a good performance and safer operation by utilizing metal phosphide and IL in SIBs. The results of this study can certainly be extended to the practical applications of large-scale SIBs, without the use of rare elements.

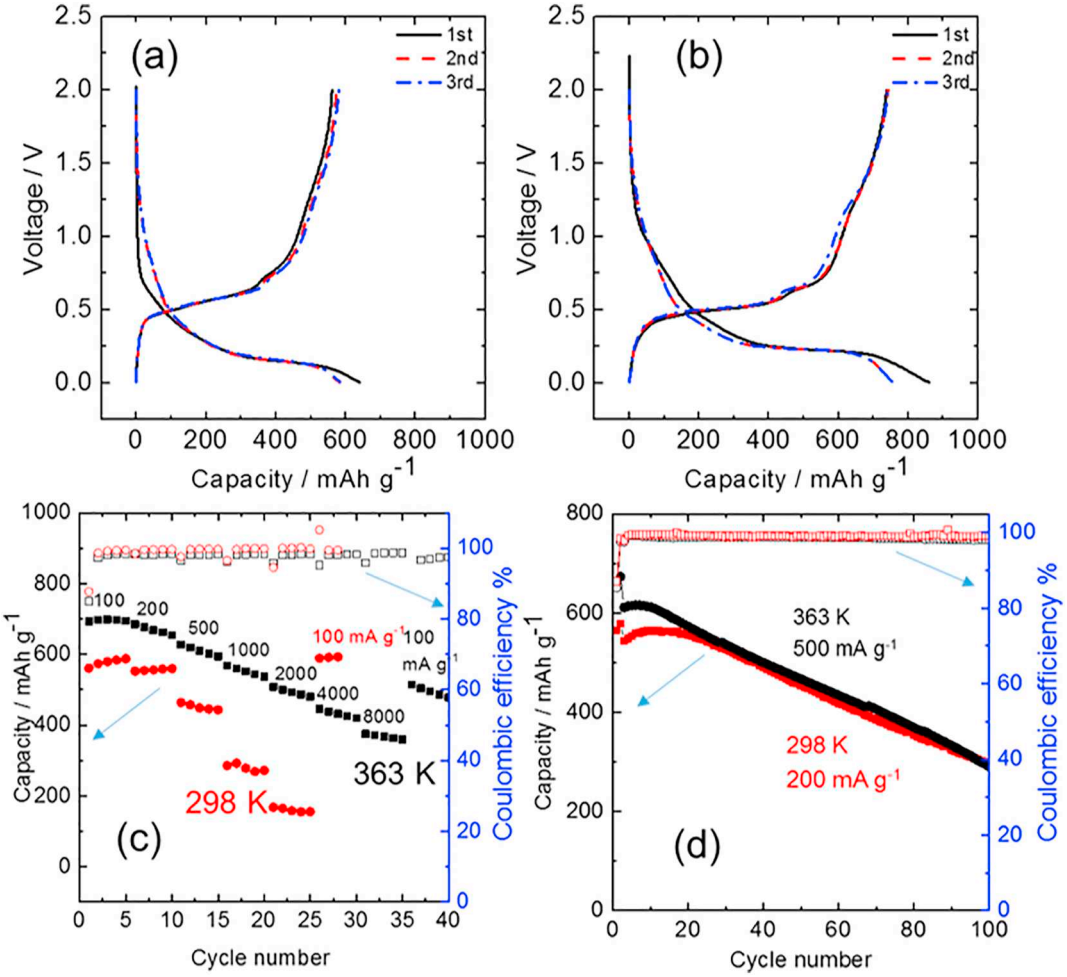

Fig. 3. Galvanostatic charge–discharge curves of the V_4P_7/5P composite electrode in IL electrolyte (half-cell configuration) at (a) 298 K and (b) 363 K (rate: 100 mA g^{-1}, voltage range: 0.005–2.000 V), (c) rate capability at 298 K and 363 K (rate: 100–8000 mA g^{-1}), and (d) cyclability at 298 K (rate: 200 mA g^{-1}) and 363 K (rate: 500 mA g^{-1}) for the first two cycles at 100 mA g^{-1}.

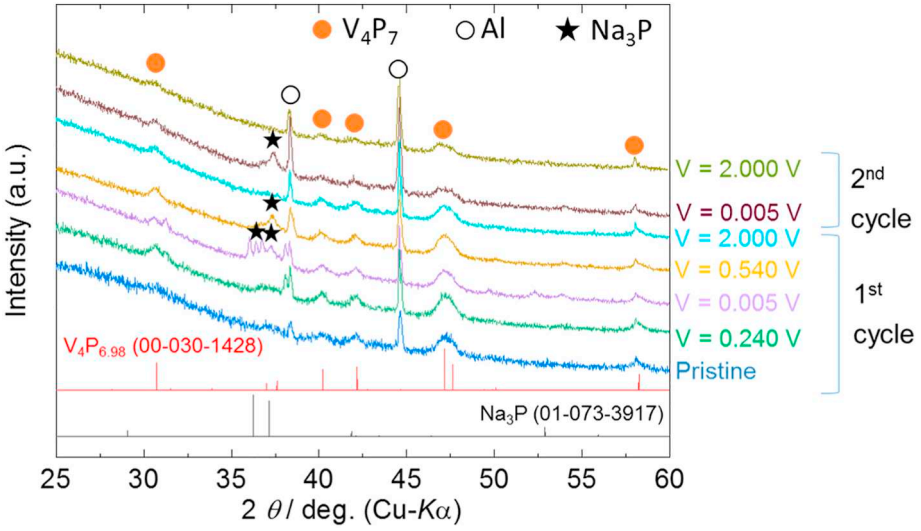

Fig. 4. Ex situ XRD patterns of the V_4P_7/5P composite obtained with IL electrolyte for the first cycle (charging: pristine, 0.24 V, 0.005 V and discharging: 0.54 V and 2 V) and second cycle (0.005 V and 2 V).

Acknowledgements

This study was partly supported by Japan Science and Technology Agency (JST) program Advanced Low Carbon Technology Research and Development Program and Japanese Ministry of Education, Culture, Sports, Science and Technology (MEXT) program Elements Strategy Initiative to Form Core Research Center.

Appendix A. Supplementary data

Supplementary data to this article can be found online at https://doi.org/10.1016/j.elecom.2019.03.014.

References

[1] V. Palomares, P. Serras, I. Villaluenga, K.B. Hueso, J. Carretero-Gonzalez, T. Rojo, Energy Environ. Sci. 5 (2012) 5884–5901.
[2] S.W. Kim, D.H. Seo, X.H. Ma, G. Ceder, K. Kang, Adv. Energy Mater. 2 (2012) 710–721.
[3] N. Yabuuchi, M. Kajiyama, J. Iwatate, H. Nishikawa, S. Hitomi, R. Okuyama, R. Usui, Y. Yamada, S. Komaba, Nat. Mater. 11 (2012) 512–517.
[4] L. Chen, M. Fiore, J.E. Wang, R. Ruffo, D.-K. Kim, G. Longoni, Adv. Sustainable Syst. 2 (2018) 1700153–1700190.
[5] J. Ni, L. Li, J. Lu, ACS Energy Lett. 3 (2018) 1137–1144.
[6] M. Fan, Y. Chen, Y. Xie, T. Yang, X. Shen, N. Xu, H. Yu, C. Yan, Adv. Funct. Mater. 26 (2016) 5019–5027.
[7] S. Kaushik, J. Hwang, K. Matsumoto, Y. Sato, R. Hagiwara, ChemElectroChem 5 (2018) 1340–1344.
[8] W. Zhang, M. Dahbi, S. Amagasa, Y. Yamada, S. Komaba, Electrochem. Commun. 69 (2016) 11–14.
[9] H. Usui, Y. Domi, R. Yamagami, K. Fujiwara, H. Nishida, H. Sakaguchi, ACS Appl. Energy Mater. 1 (2018) 306–311.
[10] H. Usui, Y. Domi, R. Yamagami, H. Sakaguchi, Green Energy & Environment, (2019) (in press).
[11] W. Li, L. Ke, Y. Wei, S. Guo, L. Gan, H. Li, T. Zhai, H. Zhoub, J. Mater. Chem. A 5 (2017) 4413–4420.
[12] S.-O. Kim, A. Manthiram, ACS Appl. Mater. Interfaces 9 (2017) 16221–16227.
[13] S.-O. Kim, A. Manthiram, Chem. Mater. 28 (2016) 5935–5942.
[14] C.-M. Park, Y.-U. Kim, H.-J. Sohn, Chem. Mater. 21 (2009) 5566–5568.
[15] F. Gillot, M. Menetrier, E. Bekaert, L. Dupont, M. Morcrette, L. Monconduit, J.M. Tarascon, J. Power Sources 172 (2007) 877–885.
[16] K.-H. Kim, C.-H. Jung, W.-S. Kim, S.-H. Hong, J. Power Sources 400 (2018) 204–211.
[17] K.-H. Kim, J. Choi, S.-H. Hong, Chem. Commun. (2019), https://doi.org/10.1039/C8CC09184F.
[18] W. Jeitschko, P.C. Donohue, V. Johnson, Acta Crystallogr. B 32 (1976) 1499–1505.
[19] H. Ohno, Electrochemical Aspects of Ionic Liquids, 2nd ed., John Wiley & Sons Inc., Hoboken, New Jersey, 2011.
[20] M. Armand, F. Endres, D.R. MacFarlane, H. Ohno, B. Scrosati, Nat. Mater. 8 (2009) 621–629.
[21] D.R. MacFarlane, N. Tachikawa, M. Forsyth, J.M. Pringle, P.C. Howlett, G.D. Elliott, J.H. Davis, M. Watanabe, P. Simon, C.A. Angell, Energy Environ. Sci. 7 (2014) 232–250.
[22] J. Hwang, K. Matsumoto, Y. Orikasa, M. Katayama, Y. Inada, T. Nohira, R. Hagiwara, J. Power Sources 377 (2018) 80–86.
[23] C. Ding, T. Nohira, R. Hagiwara, J. Power Sources 388 (2018) 19–24.
[24] Y. Domi, H. Usui, K. Yamaguchi, S. Yodoya, H. Sakaguchi, ACS Appl. Mater. Interfaces 11 (2019) 2950–2960.
[25] J. Hwang, K. Matsumoto, R. Hagiwara, Adv. Sustainable Syst. 1700171 (2018) 1–11.
[26] M. Hilder, P.C. Howlett, D. Saurel, H. Anne, M.C. Cabanas, M. Armand, T. Rojo, D.R. MacFarlane, M. Forsyth, J. Power Sources 406 (2018) 70–80.
[27] J. Hwang, K. Matsumoto, R. Hagiwara, J. Phys. Chem. C 122 (2018) 26857–26864.
[28] H. Usui, Y. Domi, H. Nishida, K. Yamaguchi, R. Yamagami, H. Sakaguchi, ChemistrySelect 3 (2018) 8462–8467.
[29] M. Dahbi, M. Fukunishi, T. Horiba, N. Yabuuchi, S. Yasuno, S. Komaba, J. Power Sources 363 (2017) 404–412.
[30] K. Matsumoto, Y. Okamoto, T. Nohira, R. Hagiwara, J. Phys. Chem. C 119 (2015) 7648–7655.
[31] M. Forsyth, H. Yoon, F. Chen, H. Zhu, D.R. MacFarlane, M. Armand, P.C. Howlett, J. Phys. Chem. C 120 (2016) 4276–4286.
[32] C.E. Myers, H.F. Franzen, J.W. Anderegg, Inorg. Chem. 24 (1985) 1822–1824.
[33] Z. Zhu, F. Liang, Z. Zhou, X. Zeng, D. Wang, P. Dong, J. Zhao, S. Sun, Y. Zhang, X. Li, J. Mater. Chem. A 6 (2018) 1513–1522.
[34] M.E. Schlesinger, Chem. Rev. 102 (2002) 4267 − 4301.